Evidence of Convective Redistribution of Carbon Monoxide in Aura Tropospheric Emission Sounder (TES) and Microwave Limb Sounder (MLS) Observations

M. Manyin, A. R. Douglass, M. R. Schoeberl

Michael Manyin
Science Systems and Applications, Inc., Lanham, Maryland, USA
Email: Michael.Manyin@nasa.gov
Address:
NASA/GSFC
Laboratory for Atmospheres
Code 613.3
Greenbelt, Maryland 20771

Anne Douglass
NASA Goddard Space Flight Center, Greenbelt, Maryland, USA
Email: Anne.R.Douglass@nasa.gov
Address:
NASA/GSFC
Laboratory for Atmospheres
Code 613.3
Greenbelt, Maryland 20771

Mark Schoeberl
Science and Technology Corporation, Hampton, Virginia, USA
Email: Mark.Schoeberl@mac.com
Address:
10005 Old Columbia Rd.
Suite M-150
Columbia, MD 21046

Abstract

Vertical convective transport is a key element of the tropospheric circulation. Convection lofts air from the boundary layer into the free troposphere, allowing surface emissions to travel much further, and altering the rate of chemical processes such as ozone production. This study uses satellite observations to focus on the convective transport of CO from the boundary layer to the mid and upper troposphere. Our hypothesis is that strong convection associated with high rain rate regions leads to a correlation between mid level and upper level CO amounts. We first test this hypothesis using the Global Modeling Initiative (GMI) chemistry and transport model. We find the correlation is robust and increases as the precipitation rate (the strength of convection) increases. We next examine three years of CO profiles from the Tropospheric Emission Sounder (TES) and Microwave Limb Sounder (MLS) instruments aboard EOS Aura. Rain rates are taken from the Tropical Rainfall Measuring Mission (TRMM) 3B-42 multi-satellite product. Again we find a correlation between mid-level and upper tropospheric CO, which increases with rain rate. Our result shows the critical importance of tropical convection in coupling vertical levels of the troposphere in the transport of trace gases. The effect is seen most clearly in strong convective regions such as the Inter-tropical Convergence Zone.

1. Introduction/Background

Convection plays a vital role in tropospheric circulation as well as the distribution of trace gases. Surface level trace gas emissions are usually mixed within the atmospheric boundary layer (BL) via turbulent diffusion but are frequently blocked from entering the free troposphere (FT) by the inversion layer at the top of the BL. Convection, along with weather fronts and orographic processes, overcome the BL inversion trapping, moving air into the FT [*Liu et al.*, 2003]. Deep convection reaches the tropopause and sometimes even overshoots into the lower stratosphere. *Cotton et al.* [1995] estimated that convective (cloud related) processes vent the mass of the boundary layer tens of times over the course of a year.

Once convection lofts constituents into the FT, they can be transported intercontinental distances because of the consistent large scale flow in that region. Convection also contributes to inter-hemispheric transport: strong convergence from the Intertropical Convergence Zone (ITCZ) convective systems can draw air from both hemispheres and loft it high enough to be pulled into the Hadley circulation. In addition to these effects on transport, convection can also dramatically alter the rate of chemical processes because of its speed. Convective time scales are very short, on the order of hours for surface to UT, as opposed to days for synoptic scale processes. The rapid transport of chemical species means that short-lived species can still reach the upper troposphere. For example, when urban air with NO_x and other ozone precursors is quickly lofted to the FT, ozone production is greatly enhanced [*Pickering*, 1992] because the transport is fast compared to the NO_x lifetime. Convective transport also extends the lifetime of some species by

reducing their exposure to loss processes in the lower troposphere; this expands their range of chemical influence [*Dickerson et al.*, 1987].

Convective processes are complex, involving surface radiative heating, updrafts from lower tropospheric levels, detrainment at heights up to and above the tropopause, condensation, latent heat release, precipitation, downdrafts and evaporative cooling (e.g. *Gamache* [1982]). Other factors include melting ice particles, and turbulent mixing due to vertical shear and gravity wave instabilities. The scale of convective systems can range from isolated thunderstorms up to mesoscale complexes measuring 1000+ km. The wide-ranging impact of convection on chemical transport makes it crucial for us to quantify convective transport and evaluate its representation in models.

Previous studies of convection have focused on various features, including (i) showing evidence of convective transport from BL to upper troposphere/lower stratosphere region [*Poulida*, 1996; *Randel and Park*, 2006; *Li et al.*, 2005; *Park et al.*, 2007; *Ricaud et al.*, 2007; *Ziemke et al.*, 2009] (ii) determining the height of convective outflow [*Gettelman and Forester*, 2002; *Froyd et al.*, 2009] (iii) identifying cases where outflow penetrates the tropopause, into the LS [*Hegglin*, 2004; *Ray et al.*, 2004; *Liu and Zipser*, 2005; *Chaboureau et al.*, 2007] (iv) comparing post-convective UT values measured by satellite to model predictions [*Liu et al.*, 2003; *Halland et al.*, 2009; *Mari et al.*, 2000] and (v) the diurnal cycle of convection [*Tian et al.*, 2004; *Liu and Zipser*, 2009].

97 One result which is especially pertinent to this study is the trimodal distribution of
98 tropical clouds, which can be traced to levels of convective detrainment. *Johnson et al.*
99 [1999] reported clouds forming at three main levels, as detected by shipborne radar
100 during the TOGA COARE experiment: low cumulus near 2 km and cumulonimbus at 15
101 to 16 km were most prominent, but cumulus congestus at approximately 5 km were
102 frequent as well. These levels correspond well with stable layers associated with the trade
103 wind inversion, the tropopause, and the 0°C melting level isotherm. Such stable levels are
104 understood to be preferential regions of convective outflow (e.g. *Zuidema* [1998]). The
105 mid-level cloud layer has also been documented by *Dessler et al.* [2006] using GLAS
106 data, and by *Haynes and Stephens* [2007] and *Riley and Mapes* [2009] with CloudSat
107 data. We will examine trace gas concentrations at the middle and upper levels of the
108 trimodal distribution, to demonstrate the effects of convective transport.
109
110 The goal of this study is to use satellite measurements of CO combined with satellite-
111 based locations of convective systems to quantify the impact of the convective systems
112 on trace gas distributions. This study uses a 3 year archive of satellite data to search for
113 evidence of convective transport of CO from the BL to mid and upper tropospheric
114 levels. Observations are restricted to the tropics, where incoming solar radiation is
115 strongest and convection is frequent. We use CO retrievals from the Tropospheric
116 Emission Sounder (TES) on EOS Aura to detect mid-level concentrations, and CO
117 retrievals from the Microwave Limb Sounder (MLS) aboard Aura for upper tropospheric
118 values. To identify areas of convective transport we use estimates of rain rate derived

119 from microwave and IR satellite measurements, calibrated with Tropical Rainfall
120 Measuring Mission (TRMM) observations, as a proxy for convective strength.
121
122 Carbon monoxide is a product of fossil fuel combustion and biomass burning, as well as
123 the oxidation of hydrocarbons, particularly methane [*Jacob*, 1999]. As such, its highest
124 concentrations are near the Earth's surface. CO is lost in the troposphere primarily by
125 reaction with the hydroxyl radical OH. The lifetime of CO generally ranges between one
126 and two months, depending on season and location within the atmosphere. Carbon
127 monoxide is not soluble and therefore not subject to rainout. These qualities make it an
128 excellent tracer. CO is monitored for many reasons, among which: it is a significant
129 anthropogenic pollutant, it is a precursor to O_3 in the troposphere, and it is a sink for OH
130 (thus modulating the oxidation of many greenhouse gases). Global CO measurements are
131 currently provided by a number of space-borne instruments, including Measurements Of
132 Pollution In The Troposphere (MOPITT) [*Drummond*, 1992] aboard the EOS Terra
133 satellite, Atmospheric Infrared Sounder (AIRS) [*McMillan et al.*, 2005] aboard EOS
134 Aqua, MLS [*Waters et al.*, 2006] and TES [*Beer et al.*, 2001], both on EOS Aura. We
135 chose to use TES and MLS in this study: TES for its sensitivity in the mid-troposphere
136 and its small footprint, allowing for unobscured profiles near or between clouds; MLS for
137 its sensitivity near the tropopause, its capability to see through clouds, and its consistent
138 proximity to TES profiles (as compared with MOPITT).
139
140 To locate convection, one must detect an accompanying phenomenon, such as clouds
141 resulting from condensing of lofted water vapor, or rainfall from those clouds. Numerous

142 approaches to cloud characterization exist, including diagnosing outgoing longwave
143 radiation (OLR) [*Liebmann and Smith*, 1996; *Lee et al.*, 2007], GOES Precipitation Index
144 (GPI) [*Arkin and Meisner*, 1987] based on microwave brightness temperatures, and
145 International Satellite Cloud Climatology Project (ISCCP) cloud classification [*Rossow*
146 *and Schiffer*, 1991] based on cloud top pressure and optical depth. Techniques such as
147 OLR and ISCCP yield high resolution products, but global coverage is only once or twice
148 a day. GPI and its derivatives use data from geosynchronous satellites for good spatial
149 and temporal resolution, but features such as high cirrus and non-raining portions of
150 cloud anvils pose difficulties.
151
152 Microwave instruments that can detect precipitation beneath clouds are quite effective at
153 locating convective rainfall. Successful estimation of rain rate from passive microwave
154 satellite data was first demonstrated with ESMR on Nimbus satellites [*Wilheit et al.*,
155 1973]. Current sensors include SSM/I on DMSP spacecraft, and TMI and PR aboard
156 TRMM. Product resolution is quite good, but coverage is incomplete.
157 Algorithms such as the TRMM 3B-42 (see section 2.2) estimate rain rates with
158 microwave data where available and calibrated IR data elsewhere, in addition to rain
159 gauge values. This provides full coverage in the low and mid latitudes, every 3 hours, at
160 quarter degree resolution. We presume that higher rain rates from the TRMM 3B-42
161 product imply greater likelihood of convection.
162
163 2. Approach
164

165 The coupling of the BL and FT by convection should have a definite signature in the
166 trace gases. CO should appear aloft following a convective event that ventilates the BL,
167 and outflow levels in the mid and upper troposphere should both show evidence of this
168 lofting transport, since detrainment preferentially occurs near the stable layers of 0°C
169 (occurring between 500 and 600 hPa) and the tropopause (~200 hPa). Thus there should
170 be higher correlation between trace gas concentrations at mid and upper tropospheric
171 levels following periods of local convective activity.
172
173 Our approach is to examine correlations between concentrations of CO in the middle and
174 upper troposphere, and relate them to proximity to significant rainfall. First we examine
175 this relationship within the context of a numerical model, the Global Modeling Initiative
176 (GMI) chemistry and transport model (CTM). Using this model will allow us to examine
177 what might be observed at the model scale of 2.5° longitude x 2° latitude. Then we
178 search for a similar relationship using data from TES and MLS on Aura. We use TES
179 pressure level 562 hPa and MLS level 215 hPa, because these correspond well with
180 convective detrainment levels put forth in the trimodal cloud characterization [*Johnson et*
181 *al.*, 1999]. We use the TRMM-calibrated 3B-42 rain rate product to identify likely
182 instances of convection.
183
184 One challenge of using TES observations is that moist convection is accompanied by
185 clouds, which prevent infrared-based remote sensing of the lower atmosphere. We
186 anticipated however that cloud-free observations of the middle troposphere would be
187 available immediately adjacent to convective areas, e.g. between clouds or along the

188 edges of convective storms. The small TES footprint makes this approach reasonable.
189 We anticipate only a small fraction of the ~650 measurements made in the tropics (18°N-
190 S) during each global survey will meet our criteria for cloud amount and proximity to
191 convection. We compensate for infrequency by drawing upon a multi-year archive.
192
193 The remainder of the paper is structured as follows: The models (CTM and AGCM) are
194 discussed in section 2.1; the data sources for CO and rain rate are presented in 2.2.
195 Results are given in section 3, and conclusions follow in section 4.
196
197 2.1 GMI and GEOS-4
198
199 NASA's Global Modeling Initiative has developed a 'Combo' CTM that combines
200 photochemical schemes that are appropriate for the stratosphere and troposphere. The
201 Combo CTM may be driven by meteorological fields from a general circulation model
202 (GCM) or from a data assimilation system (DAS). GMI Combo includes gas phase
203 reactions, photolysis, wet scavenging, dry deposition, heterogeneous chemistry (PSCs)
204 and emissions [*Strahan et al.*, 2007; *Duncan et al.*, 2007]. For this study we have used
205 the "Aura4" GMI experiment, run at 2° latitude by 2.5° longitude, with 55 vertical levels
206 (hybrid sigma-pressure) up to 0.015 hPa. We use simulated CO that is recorded at times
207 corresponding to the Aura afternoon overpass times, between 1 and 2 p.m. local time to
208 best match the observation times of TES on Aura.
209

For the Aura4 experiment, GMI 'Combo' used meteorological fields taken from the Goddard Earth Observing System Data Assimilation System (GEOS DAS) version 4 [*Bloom et al.*, 2005]. The GEOS DAS fields are produced at 1° latitude by 1.25° longitude on 55 levels; the fields are adapted for use at 2° by 2.5° in the CTM. The physics parameterization scheme consists of parameterizations for precipitation, clouds/radiation, turbulent mixing, and surface processes. The deep moist convection scheme is that of *Zhang and McFarlane* [1995], which uses a plume ensemble approach with convective updrafts and related downdrafts. Shallow convection is covered by the *Hack* [1994] scheme.

GEOS-4 DAS assimilates observations from many sources, including SSM/I (total precipitable water), MODIS (winds), geosynchronous satellites (winds), TOVS sounders (temperature and moisture), ERS-2 and QuikScat (sea-level winds), along with rawinsondes (temperature, winds, moisture), and surface stations (temperature, pressure, winds). The DAS outputs dozens of fields, including those that GMI requires, such as winds, temperature, precipitation and convective mass flux. Fields are saved at three hour intervals, in instantaneous and time-averaged forms; GMI 'Combo' uses the latter, horizontally averaged to 2° x 2.5°. In order to identify grid boxes with convective activity, we used the GEOS-4 DAS output field "PRECON", which stores the convective precipitation rate. Each GEOS-4 output file covers a single synoptic time period. In order to match the local ascending Aura overpass times implicit in each GMI output file, the convective precipitation field had to be extracted from multiple GEOS-4 files covering 24 hours of simulation.

233

234 2.2 TES, MLS and TRMM (3B-42)

235

236 The Tropospheric Emission Spectrometer (TES) is a Fourier transform spectrometer
237 [*Beer et al.*, 2001; *Beer*, 2006]. It is one of several instruments aboard NASA's Aura
238 satellite, positioned in an ascending sun synchronous orbit with equator crossing at about
239 13:45 local solar time. TES measures in the infrared to detect trace gases including CO,
240 water vapor, O_3 and methane. This study uses nadir profiles acquired during TES Global
241 Surveys. Nadir view operates with a 5.3 x 8.3 km footprint, and each profile in a Level 2
242 file consists of data on 65 pressure levels ranging from nominal surface pressure to 0.1
243 hPa. Compared to the GMI model, TES has a much higher horizontal resolution, but of
244 course the TES observations are much sparser than the GMI output (e.g. 9800 tropical
245 profiles in July 2007, compared with 84,816 GMI gridbox values). And in terms of
246 vertical resolution, the model levels within a grid column are independent compared to
247 low vertical resolution retrieved TES profiles.

248

249 In the tropics, a TES tropospheric CO profile typically has between 1 and 2 degrees of
250 freedom (DOF), a measure of the number of "independent" pieces of information that
251 contributed to that profile. These pieces of information are used to modify the a priori
252 (first guess) trace gas profile. (See *Beer* [2006] for an overview.) With a greater number
253 of DOFs it is possible to achieve more variation from the a priori. In December 2005,
254 TES implemented an Optical Bench warmup which resulted in better instrument

255 alignment, and average DOF values for TES CO measurements were significantly
256 improved. For this reason, we have only used data from January 2006 forward.
257
258 As a consequence of variations in TES DOF, some measurements reflect the actual state
259 of the atmosphere, while others rely heavily on the a priori. To distinguish between such
260 cases we consult the averaging kernel diagonal (AKD) values; where these are high
261 (close to 0.1), there is greater confidence that the true atmospheric values are retrieved
262 [*Halland et al.*, 2009]. We tested several AKD thresholds and use an AKD threshold of
263 0.085 for most of this paper. In the final figure we show results using two other
264 thresholds for the AKD.
265
266 TES profiles used in this study were Level 2, Version 4. They were filtered using the
267 quality control fields, as in Table 5-3 of the *EOS TES L2 Data User's Guide* [*Osterman*
268 *et al.*, 2008]. In addition, since the TES IR-based retrievals are subject to interference by
269 clouds, profiles with nominal cloud top pressures less than 572 hPa were discarded. We
270 used profiles between 18°N and 18°S because DOFs changed abruptly beyond those
271 boundaries due to changes in the a priori.
272
273 The MLS instrument aboard Aura measures profiles of radiance from the Earth's limb
274 from upper troposphere to the mesosphere [*Waters*, 2006]. MLS scans columns ahead of
275 the satellite, every 165km along its orbit. MLS measures CO [*Livesey et al.*, 2006;
276 *Pumphrey et al.*, 2007], along with a dozen other atmospheric trace gases. As a

277 microwave instrument, it can detect constituents despite the presence of aerosols, cirrus
278 or polar stratospheric clouds.
279
280 In this study we use CO as reported by MLS (version 2.2) at 215 hPa. At this level, the
281 CO morphology and variability are adequately measured, but the values are biased by
282 approximately a factor of 2 [*Livesey et al.*, 2008]. We compensate by dividing all values
283 in half; we also processed the data according to guidelines in the MLS data quality
284 document [*Livesey et al.*, 2007]. Each MLS CO profile was paired with the closest TES
285 profile; the average separation was 195 km, and the average time difference was
286 approximately 7 minutes.
287
288 For rain rate data, we turned to the 3B-42 product from the Tropical Rainfall Measuring
289 Mission (TRMM) [*Simpson et al.*, 1996]. This mission, a joint effort of the United States
290 and Japan, was launched in 1997. It supports several instruments including the TRMM
291 Microwave Imager (TMI), the Precipitation Radar (PR), and the Visible and Infrared
292 Scanner (VIRS) [*Kummerow et al.*, 1998]. The 3B-42 algorithm [*Huffman et al.*, 2007]
293 combines observations from several satellites, including TRMM, with rain gauge
294 analyses. Computation of the multi-satellite portion begins with a merged microwave
295 product including TMI and SSM/I rain rate estimates. Then VIRS data is used to produce
296 an infrared/rain rate relationship, which is applied to geosynchronous IR data, such as
297 that from the Geostationary Operational Environmental Satellite (GOES) series. The
298 microwave products are high resolution (e.g. TMI is 5.1 km), but measurements
299 accumulated over timescales of up to three hours do not completely cover the tropics.

The IR measurements are similar resolution (e.g. GOES is 4 km), and a merged product from several geo-IR satellites provides excellent coverage (60° N-S) at half hour intervals [*Janowiak et al.*, 2001]. Incorporating both microwave and IR data, the 3B-42 rain rate product is generated for latitudes covered by TRMM (50° N-S) at quarter degree resolution and 3 hour intervals.

3B-42 does not distinguish between convective rain, which is linked to strong vertical transport, and stratiform rain, which is not. However, it is generally true that greater rain rates are more likely associated with convective systems. Indeed, the ratio of convective to stratiform rain rates in the tropics is 4.1, when measured at PR resolution [*Schumacher and Houze*, 2003]. So the error introduced by the inclusion of stratiform rain rates in this study should be relatively small.

Rain rates were used as follows: For a given pair of TES and MLS CO profiles we searched a neighborhood of 3B-42 grid boxes centered on the spot midway between the profiles. Since 3B-42 rain rates are available every three hours, we used the values from the 3-hour window prior to the TES observation, to ensure that we would see the effects of vertical mixing.

3. Results

3.1 GMI and GEOS-4

We first analyze simulated upper and mid-tropospheric CO to demonstrate the expected relationship between composition and convective transport as implemented in the GMI CTM.

3.1.1 Scatter plots varying rain rate threshold

Daily GMI CO concentrations from July 2007 were compared at two different pressure levels, 562 hPa and 215 hPa, selected to match the TES and MLS pressure levels used in the next section. The 562 hPa level represents the level of expected convective detrainment around the 0°C isotherm, while 215 hPa corresponds with outflow near the tropopause. As shown in the first scatter plot of Figure 1, the majority of CO values on both pressure levels range between 50 and 150 ppbv. Panel (a) includes values from all GMI grid boxes in the tropics, 19°S - 19°N, regardless of rain rate. The broad pattern matches our expectations: Points along the diagonal are consistent with vertical convective transport to both levels of the troposphere; areas with substantial CO at lower altitudes but minimal amounts above may represent cases where shallow convection has deposited CO emissions from the boundary layer up into the mid-troposphere. Areas with greater CO concentrations at 215 hPa may represent cases where deep convection has been dominant. The off-diagonal cases could also be due to the effects of horizontal advection transporting CO from other convective areas.

Figure 1, panels (b)-(d) show subsets of the original data, where profiles were discarded if the convective rain rate was less than 0.5, 1.0 and 2.0 mm/hr respectively. As

346 convective activity increases from one panel to the next, profiles with markedly different
347 CO concentrations at the two levels are eliminated. This fits with our hypothesis, in that
348 convective transport is coupling the middle and upper levels of the troposphere. In the
349 last panel, where convective rain rates are highest, the remaining points are clustered
350 along the diagonal, and the correlation coefficient is quite high, at 0.967. This simple test
351 demonstrates that the GMI implementation of trace gas transport, as driven by GEOS-4
352 winds and convective mass flux, is consistent with our conceptual model of the effect
353 vertical convective mixing will have on the trace gas distributions. This is an idealized
354 case with which to compare the TES/MLS observations.
355
356 3.1.2 Geographic Location of GEOS-4 Rain
357
358 Another useful plot for comparing the model and satellite results is the geographic
359 location of dominant rainfall. The areas of convective rain in the GEOS-4 DAS are
360 shown in Figure 2. The grid boxes are shaded based on the number of days that met or
361 exceeded the rain rate threshold. Note the prominence of the ITCZ in panels (a) and (b),
362 and the areas of most frequent convective rain such as Costa Rica and north of Papua
363 New Guinea, in panel (c). These plots confirm the success of GEOS-4 DAS in
364 reproducing realistic rain distribution patterns.
365
366 3.2 TES, MLS and TRMM (3B-42)
367

368 The TES and MLS observations are quite sparse in comparison to model output. Within
369 our constraints of tropical latitudes and sufficiently cloud-free observations, a month of
370 TES Global Survey data yields roughly 30 to 60 profiles. Filtering these using rain rate
371 thresholds quickly reduces the sample size to numbers too small for a meaningful
372 analysis. So we chose to include three full years of TES and MLS data in this study,
373 from 2006 through 2008.
374
375 In order to estimate the strength of convection in the neighborhood of TES and MLS
376 measurements, we consulted the TRMM-calibrated rain rate data for the 3-hour interval
377 prior to the TES overpass time. Our initial tests included an area similar in size to a GMI
378 gridbox: we searched an 11x7 patch of TRMM values centered between the TES and
379 MLS profiles, and took the maximum rain rate. (Since TRMM 3B-42 is 0.25° resolution,
380 the area was 2.75° in longitude by 1.75° in latitude.) In addition we tested our approach
381 with smaller patches of TRMM grid boxes, including 7x5, 5x3 and 3x3. As the area in
382 which we searched for rain grew smaller, the effects of the vertical mixing became more
383 apparent. So we begin by examining the 3x3 case, wherein each patch is a square of 9
384 grid boxes; the maximum rain rate is sought within a 0.75° x 0.75° region.
385
386 3.2.1 Scatter plots varying rain rate thresholds
387
388 Plots of CO correlation between pressure levels 562 and 215 hPa are shown in Figure 3.
389 Panel (a) includes all qualifying profiles, regardless of local rain rate. It shows that the
390 majority of values at midlevel are between 50 and 150 ppbv, while the range on the upper

391 level is between 50 and 125 ppbv. The (solid) line of linear fit shows that greater CO
392 concentrations exist at lower altitudes. This can be attributed to diffusive transport from
393 the boundary layer, particularly during times of weak trade inversion. It may also be due
394 in part to the approximate correction we have applied to compensate for the MLS high
395 bias. Greater CO concentrations at mid-level were also present in GMI (see the line of
396 linear fit in Figure 1), but in the TES/MLS case this is much more pronounced.
397
398 Panels (b)-(d) in Figure 3 show the relationship between middle and upper tropospheric
399 CO as the rain rate requirement for the TES/MLS observation neighborhood is increased.
400 As the threshold is increased from 1 up to 3 mm/hr, the correlation steadily increases as
401 well. TES/MLS values associated with higher rain rates are clustered around the
402 diagonal, as was the case in the GMI plots (Figure 1). Clustering is tighter for GMI,
403 because values are reported immediately after the convective mass flux is applied to the
404 trace gas field, as opposed to the TES/MLS measurements which were taken up to 6
405 hours after rainfall. The interval between convective rain and CO observations gives
406 advection time to alter distributions.
407
408 Part of the difficulty in characterizing patterns in this data is the remarkably low number
409 of profiles satisfying our criteria, as shown in Table 1. This is due in part to the rejection
410 of cloudy TES profiles. For the 0 mm/hr case, 84% of the profiles were filtered out based
411 on their cloud top pressure. In the case of 3 mm/hr, 90% were removed. The linkage of
412 additional clouds with higher rain rate was expected, since convective rain is
413 accompanied by updrafts, leading to detrainment, condensation, and therefore clouds.

To establish a level of confidence in the correlation values computed for small sample sizes, we employed a bootstrap approach: we computed the correlation for a randomly chosen subset of half the points, repeated this process 1000 times, and made histograms of the results. We accepted the correlation over the full sample only when it matched the average of the bootstrap correlations to within 0.05, and when the central 90% of the bootstrap values did not exceed a range of 0.5. Each of the correlations listed in Table 1 satisfied these criteria. The bootstrap histograms are shown as insets in Figure 3, with markers denoting the 5%, 95% and average values.

3.2.2 Geographic Location of TES/MLS Observations

Because strong convection is usually accompanied by substantial clouds, we anticipated that non-cloudy TES profiles linked with higher rain rates would be adjacent to regions of heavy rain, rather than within such regions. The locations of accepted TES/MLS profile pairs are shown in Figure 4. In panel (a), rain rates are not considered, and the pattern arises solely from the elimination of cloudy profiles. The areas of highest number of observations are those that tend to have low levels of rain, such as Saudi Arabia and the horn of Africa. The fewest profiles are found in areas of high rainfall, such as the ITCZ, Maritime Continent, Indian Ocean and Brazil. So, as expected, most non-cloudy TES observations are in the areas of least convective rain. Once a rain rate threshold is applied a different pattern emerges. (Note that the color scale for panels (b) and (c) is different from that in the first panel.) As anticipated, the profiles in rainy neighborhoods

437 tend to be located adjacent to areas of frequent rain, such as the ITCZ, Brazil, and the
438 Indian Ocean. We interpret these to be instances where TES measures CO in sufficiently
439 cloud-free columns along the edges of convective storm systems. The convective lofting
440 of CO by such systems is evident in the TES and MLS data. With higher rain rates there
441 is greater likelihood of convective activity in the area, and therefore greater vertical
442 mixing of CO and higher correlation between levels.
443
444 3.2.3 Correlation affected by size of TRMM neighborhood, and AK Diagonal
445
446 How does the correlation between mid and upper levels of CO change as the distance
447 from convection increases? And how is the correlation affected by our choice of AKD
448 threshold? To answer these questions, we performed two sensitivity experiments. First
449 we varied the size of the search neighborhood in the TRMM-based rain rate data, testing
450 four different patch sizes: 11x7, 7x5, 5x3 and 3x3 grid boxes, in the 0.25° x 0.25° grid.
451 Larger search areas allow for rain rate maxima to be identified at greater distances from
452 the CO profiles. In the second sensitivity test we varied the minimum TES AKD
453 accepted: 0.08, 0.085 and 0.09. This was done to determine the trend in correlations as
454 TES values gained greater independence from the a priori and more accurately reflected
455 the state of the atmosphere. The results from both of these experiments are shown in
456 Figure 5. Multiple patch sizes are plotted in each panel, and a different minimum AKD
457 applies to each panel. (Note that the original series of correlations, recorded in Table 1,
458 appears as the sequence of red asterisks in the middle panel.)
459

460 The influence of TRMM search area size is evident in panel (a). Each gray square
461 designates the CO correlation derived from TES/MLS profile pairs close to a sufficiently
462 high TRMM rain rate, determined by searching an 11x7 neighborhood of TRMM values
463 (2.75° x 1.25°). The blue triangles show the results from searching smaller
464 neighborhoods of 7x5 grid boxes (1.75° x 1.25°). The green diamonds reflect 5x3 patches
465 (1.25° x 0.75°), and the red asterisks use 3x3 patches (0.75° x 0.75°).
466 As the search area is constricted, the average distance between the TES/MLS profiles and
467 maximum rain rate is reduced, so the lofting effects of convection should be more evident
468 in the CO measurements, and we anticipated higher correlation as a result. This is clearly
469 exhibited in the plots; while the 11x7 sequence does not show an increase in correlation
470 as local maximum rain rate increases, the 7x5 sequence does show this relationship, and
471 the 5x3 and 3x3 cases even more so. This demonstrates that trace gas correlation between
472 the middle and upper troposphere depends on proximity to convection as well as
473 convective intensity.
474
475 The series of three panels shows the impact of more stringent TES AKD requirements.
476 Two effects are apparent. First, as average AKD increases, the CO correlation for a given
477 rain rate tends to increase as well. This means that the trends we are seeing derive
478 primarily from the atmospheric state, and should not be attributed to the TES a priori.
479 The second effect is the reduction in qualified TES profiles, resulting in smaller sample
480 sizes over which to evaluate correlations. This paucity of data is further exacerbated
481 when profiles are filtered based on rain rate. With TES AKD $\geq$ 0.08, before rain rate is
482 considered, there are 17,358 profile pairs from the 2006-2008 period; with AKD $\geq$ 0.085

there are 9,945 pairs, and with AKD $\geq$ 0.09 only 5,091 pairs qualify. Filtering these sets with increasing rain rate thresholds quickly reduces the sample sizes to fewer than 50, and soon thereafter the bootstrap confidence test (see section 3.2.1) begins to fail, discontinuing each sequence. For example, the 3x3 sequence in panel (c) is computed for rain rates at or above 0, 0.5 and 1.0 mm/hr, using 5,091, 83 and 41 profile pairs respectively. At 1.5 mm/hr, too few profiles remain to calculate a statistically meaningful correlation. We assert that, despite the short series of correlations plotted in the last panel, they confirm the trends seen in the prior two panels, namely that the proximity and intensity of convection influences the degree of correlation in middle and upper tropospheric concentrations of CO.

4. Conclusion

Using rain activity as a proxy for convection we have demonstrated a link between tropical convection and CO concentrations in the middle and upper troposphere, at levels corresponding to the stable layers at 0°C and the tropopause. In other words, convective activity is pumping CO from the surface into the mid and upper troposphere – chemically coupling the tropospheric layers. This association was first demonstrated in the GMI CTM. Correlations between CO concentrations at 562 and 215 hPa increased as the convective precipitation rate increased. This conformed to our expectations. In addition, the locations of high convective rain rates for the month we studied aligned well with standard patterns of tropical rain, e.g. the ITCZ.

506 For the observational study, CO measurements from TES at 562 hPa (unobscured by
507 clouds) and from MLS at 215 hPa were examined, together with rain rates from the
508 TRMM 3B-42 product. First we examined the influence of rain rate on the correlation,
509 using a 0.75 x 0.75 search area within TRMM data for each pair of TES/MLS profiles,
510 and using TES profiles with at least an AKD value of 0.085. As the rain rate threshold
511 was increased, the correlation between CO burdens at the two levels grew stronger, as we
512 anticipated; greater convective vertical mixing is concomitant with heavier rain.
513 However, the sample size (profile count) fell dramatically as we restricted ourselves to
514 higher local rain rates. This was because rain is accompanied by clouds (convective rain
515 leads to additional cloud formation), and we discarded TES profiles that were not
516 sufficiently cloud-free.
517
518 The influence of clouds was also evident in the location of qualifying profiles. Most
519 profiles clustered in areas of minimal rain, such as the horn of Africa. When rain rate
520 thresholds were enforced, the remaining profiles appeared at the periphery of major
521 cloudy areas such as the ITCZ and Brazil. These plots differed greatly from the GMI
522 location plots, principally due to the cloud-free condition we imposed on TES profiles.
523 Fortunately, the small footprint of TES permitted some measurements not obscured by
524 clouds immediately adjacent to regions with rain. We extended the study to include 36
525 months of data to provide a sufficient number of non-cloudy profiles. Also we used a
526 bootstrap statistical method to gauge confidence in cases with only a small number of CO
527 measurements. By these means we were able to show linkage between rain rate and CO
528 burden correlation similar to that shown with the model.

529

530 We explored the sensitivity of this result to two parameters: the rain search area, and the
531 TES averaging kernel diagonal values. For the former, we varied the extent of search
532 within TRMM 3B-42 for a maximum rain rate to associate with each TES/MLS profile
533 pair. TRMM data neighborhoods of four sizes, ranging from 2.75°x1.75° (approximately
534 the size of one GMI gridbox), to 0.75°x0.75° were tested. For each areal size, our first
535 result was reproduced: increased rain rates led to higher correlations. Smaller search
536 domains also tended to yield better correlations, particularly for greater rain rates. This
537 result is consistent with the idea that closer proximity to convective mixing translates into
538 a stronger observable signal. When we required higher AKD values for TES, the
539 correlations again tended to rise, giving us confidence that the signal in CO reflected
540 actual atmospheric concentrations, rather than strong influence from the a priori. We
541 showed significant correlations up to AKD threshold 0.09, beyond which the profile
542 count was too small for meaningful results.

543

544 We have demonstrated that tropical convection plays an important role in transporting
545 trace gases vertically within the troposphere, with effects in keeping with the trimodal
546 characterization of tropical clouds, in which boundary layer parcels are convectively
547 lofted to stable levels in the troposphere. Satellite observations show that this process
548 operates on a wide scale throughout the tropical regions where strong convection is
549 prevalent.

550

In this paper we examined how correlation was affected by proximity to rainfall but subsequent advection of the CO plume was not considered. A follow-up study could focus on cases where convection was located upwind of the CO measurement.

Acknowledgements

We would like to thank Susan Strahan for her assistance with GMI, and George Huffman who provided guidance on using the TRMM 3B-42 product.

The TES data were obtained from the NASA Langley Research Center Atmospheric Sciences Data Center.

References

Arkin, P. A., and B. N. Meisner (1987), THE RELATIONSHIP BETWEEN LARGE-SCALE CONVECTIVE RAINFALL AND COLD CLOUD OVER THE WESTERN-HEMISPHERE DURING 1982-84, *Monthly Weather Review*, *115*(1), 51-74.

Beer, R. (2006), TES on the Aura mission: Scientific objectives, measurements, and analysis overview, *Ieee Transactions on Geoscience and Remote Sensing*, *44*(5), 1102-1105, DOI:10.1109/tgrs.2005.863716.

574

575 Beer, R., T. A. Glavich, and D. M. Rider (2001), Tropospheric emission spectrometer for
576 the Earth Observing System's Aura Satellite, *Applied Optics*, *40*(15), 2356-2367.

577

578 Bloom, S., et al. (2005), Documentation and Validation of the Goddard Earth Observing
579 System (GEOS) Data Assimilation System-Version 4 *Rep.*

580

581 Chaboureau, J. P., J. P. Cammas, J. Duron, P. J. Mascart, N. M. Sitnikov, and H. J.
582 Voessing (2007), A numerical study of tropical cross-tropopause transport by convective
583 overshoots, *Atmospheric Chemistry and Physics*, *7*(7), 1731-1740.

584

585 Cotton, W. R., G. D. Alexander, R. Hertenstein, R. L. Walko, R. L. McAnelly, and M.
586 Nicholls (1995), Cloud venting - A review and some new global annual estimates, *Earth-*
587 *Science Reviews*, *39*(3-4), 169-206.

588

589 Dessler, A. E., S. P. Palm, and J. D. Spinhirne (2006), Tropical cloud-top height
590 distributions revealed by the Ice, Cloud, and Land Elevation Satellite
591 (ICESat)/Geoscience Laser Altimeter System (GLAS), *Journal of Geophysical Research-*
592 *Atmospheres*, *111*(D12), 11, DOI: D12215 10.1029/2005jd006705.

593

594 Dickerson, R. R., et al. (1987), THUNDERSTORMS - AN IMPORTANT
595 MECHANISM IN THE TRANSPORT OF AIR-POLLUTANTS, *Science*, *235*(4787),
596 460-464.

Drummond, J. R. (1992), Measurements of Pollution in the Troposphere (MOPITT)*Rep.*, 77-101 pp, North-Holland, Amsterdam.

Duncan, B. N., S. E. Strahan, Y. Yoshida, S. D. Steenrod, and N. Livesey (2007), Model study of the cross-tropopause transport of biomass burning pollution, *Atmospheric Chemistry and Physics*, *7*(14), 3713-3736.

Froyd, K. D., D. M. Murphy, T. J. Sanford, D. S. Thomson, J. C. Wilson, L. Pfister, and L. Lait (2009), Aerosol composition of the tropical upper troposphere, *Atmospheric Chemistry and Physics*, *9*(13), 4363-4385.

Gamache, J. F., and R. A. Houze (1982), MESOSCALE AIR MOTIONS ASSOCIATED WITH A TROPICAL SQUALL LINE, *Monthly Weather Review*, *110*(2), 118-135.

Gettelman, A., and P. M. D. Forster (2002), A climatology of the tropical tropopause layer, paper presented at International Symposium on Stratospheric Variations and Climate, Fukuoka, Japan, Nov 12-15.

Hack, J. J. (1994), Parameterization of moist convection in the National Center for Atmospheric Research community climate model (CCM2), *Journal of Geophysical Research-Atmospheres*, *99*(D3), 5551-5568.

620 Halland, J. J., H. E. Fuelberg, K. E. Pickering, and M. Luo (2009), Identifying convective
621 transport of carbon monoxide by comparing remotely sensed observations from TES with
622 cloud modeling simulations, *Atmospheric Chemistry and Physics*, *9*(13), 4279-4294.
623
624 Haynes, J. M., and G. L. Stephens (2007), Tropical oceanic cloudiness and the incidence
625 of precipitation: Early results from CloudSat, *Geophysical Research Letters*, *34*(9), 5,
626 DOI: L09811 10.1029/2007gl029335.
627
628 Hegglin, M. I., et al. (2004), Tracing troposphere-to-stratosphere transport above a mid-
629 latitude deep convective system, *Atmospheric Chemistry and Physics*, *4*, 741-756.
630
631 Huffman, G. J., R. F. Adler, D. T. Bolvin, G. J. Gu, E. J. Nelkin, K. P. Bowman, Y.
632 Hong, E. F. Stocker, and D. B. Wolff (2007), The TRMM multisatellite precipitation
633 analysis (TMPA): Quasi-global, multiyear, combined-sensor precipitation estimates at
634 fine scales, *Journal of Hydrometeorology*, *8*(1), 38-55, DOI: 10.1175/jhm560.1.
635
636 Jacob, D. J. (1999), *Introduction to Atmospheric Chemistry*, Princeton University Press,
637 Princeton, New Jersey.
638
639 Janowiak, J. E., R. J. Joyce, and Y. Yarosh (2001), A real-time global half-hourly pixel-
640 resolution infrared dataset and its applications, *Bulletin of the American Meteorological*
641 *Society*, *82*(2), 205-217.
642

643 Johnson, R. H., T. M. Rickenbach, S. A. Rutledge, P. E. Ciesielski, and W. H. Schubert
644 (1999), Trimodal characteristics of tropical convection, *Journal of Climate*, *12*(8), 2397-
645 2418.
646
647 Kummerow, C., W. Barnes, T. Kozu, J. Shiue, and J. Simpson (1998), The Tropical
648 Rainfall Measuring Mission (TRMM) sensor package, *Journal of Atmospheric and*
649 *Oceanic Technology*, *15*(3), 809-817.
650
651 Lee, H. T., A. Gruber, R. G. Ellingson, and I. Laszlo (2007), Development of the HIRS
652 outgoing longwave radiation climate dataset, *Journal of Atmospheric and Oceanic*
653 *Technology*, *24*(12), 2029-2047, DOI: 10.1175/2007jtecha989.1.
654
655 Li, Q. B., et al. (2005), Convective outflow of South Asian pollution: A global CTM
656 simulation compared with EOS MLS observations, *Geophysical Research Letters*,
657 *32*(14), DOI: L14826 10.1029/2005gl022762.
658
659 Liebmann, B., and C. A. Smith (1996), Description of a complete (interpolated) outgoing
660 longwave radiation dataset, *Bulletin of the American Meteorological Society*, *77*(6),
661 1275-1277.
662
663 Liu, C. T., and E. J. Zipser (2005), Global distribution of convection penetrating the
664 tropical tropopause, *Journal of Geophysical Research-Atmospheres*, *110*(D23), DOI:
665 D23104 10.1029/2005jd006063.

Liu, C. T., and E. J. Zipser (2009), Implications of the day versus night differences of water vapor, carbon monoxide, and thin cloud observations near the tropical tropopause, *Journal of Geophysical Research-Atmospheres*, *114*, 14, DOI: D09303 10.1029/2008jd011524.

Liu, H. Y., D. J. Jacob, I. Bey, R. M. Yantosca, B. N. Duncan, and G. W. Sachse (2003), Transport pathways for Asian pollution outflow over the Pacific: Interannual and seasonal variations, *Journal of Geophysical Research-Atmospheres*, *108*(D20), DOI: 8786 10.1029/2002jd003102.

Livesey, N. J., W. Van Snyder, W. G. Read, and P. A. Wagner (2006), Retrieval algorithms for the EOS Microwave Limb Sounder (MLS), *Ieee Transactions on Geoscience and Remote Sensing*, *44*(5), 1144-1155, DOI: 10.1109/tgrs.2006.872327.

Livesey, N. J., et al. (2007), Earth Observing Systems (EOS) Microwave Limb Sounder (MLS) Version 2.2 level 2 data quality and description document, version 2.2x-1.0a*Rep.*, Jet Propulsion Laboratory / California Institute of Technology, Pasadena, California.

Livesey, N. J., et al. (2008), Validation of Aura Microwave Limb Sounder O-3 and CO observations in the upper troposphere and lower stratosphere, *Journal of Geophysical Research-Atmospheres*, *113*(D15), DOI: D15s02 10.1029/2007jd008805.

689 Mari, C., D. J. Jacob, and P. Bechtold (2000), Transport and scavenging of soluble gases
690 in a deep convective cloud, *Journal of Geophysical Research-Atmospheres*, *105*(D17),
691 22255-22267.
692
693 McMillan, W. W., C. Barnet, L. Strow, M. T. Chahine, M. L. McCourt, J. X. Warner, P.
694 C. Novelli, S. Korontzi, E. S. Maddy, and S. Datta (2005), Daily global maps of carbon
695 monoxide from NASA's Atmospheric Infrared Sounder, *Geophysical Research Letters*,
696 *32*(11), DOI: L11801 10.1029/2004gl021821.
697
698 Osterman, G. (editor), et al. (July 31, 2008), Earth Observing System (EOS)
699 Tropospheric Emission Spectrometer (TES) Level 2 (L2) Data User's Guide (Up to &
700 including Version F04_04 data), Jet Propulsion Laboratory, Pasadena, California.
701
702 Park, S., et al. (2007), The CO2 tracer clock for the Tropical Tropopause Layer,
703 *Atmospheric Chemistry and Physics*, *7*(14), 3989-4000.
704
705 Pickering, K. E., A. M. Thompson, J. R. Scala, W. K. Tao, R. R. Dickerson, and J.
706 Simpson (1992), FREE TROPOSPHERIC OZONE PRODUCTION FOLLOWING
707 ENTRAINMENT OF URBAN PLUMES INTO DEEP CONVECTION, *Journal of*
708 *Geophysical Research-Atmospheres*, *97*(D16), 17985-18000.
709

710 Poulida, O., R. R. Dickerson, and A. Heymsfield (1996), Stratosphere-troposphere
711 exchange in a midlatitude mesoscale convective complex, *Journal of Geophysical*
712 *Research-Atmospheres*, *101*(D3), 6823-6836.
713
714 Pumphrey, H. C., et al. (2007), Validation of middle-atmosphere carbon monoxide
715 retrievals from the Microwave Limb Sounder on Aura, *Journal of Geophysical Research-*
716 *Atmospheres*, *112*(D24), DOI: D24s38 10.1029/2007jd008723.
717
718 Randel, W. J., and M. Park (2006), Deep convective influence on the Asian summer
719 monsoon anticyclone and associated tracer variability observed with Atmospheric
720 Infrared Sounder (AIRS), *Journal of Geophysical Research-Atmospheres*, *111*(D12),
721 D12314 10.1029/2005jd006490.
722
723 Ray, E. A., et al. (2004), Evidence of the effect of summertime midlatitude convection on
724 the subtropical lower stratosphere from CRYSTAL-FACE tracer measurements, *Journal*
725 *of Geophysical Research-Atmospheres*, *109*(D18), DOI: D18304 10.1029/2004jd004655.
726
727 Ricaud, P., B. Barret, J. L. Attie, E. Motte, E. Le Flochmoen, H. Teyssedre, V. H. Peuch,
728 N. Livesey, A. Lambert, and J. P. Pommereau (2007), Impact of land convection on
729 troposphere-stratosphere exchange in the tropics, *Atmospheric Chemistry and Physics*,
730 *7*(21), 5639-5657.
731

732 Riley, E. M., and B. E. Mapes (2009), Unexpected peak near-15 degrees C in CloudSat
733 echo top climatology, *Geophysical Research Letters*, *36*, 5, DOI: L09819
734 10.1029/2009gl037558.
735
736 Rossow, W. B., and R. A. Schiffer (1991), ISCCP CLOUD DATA PRODUCTS, *Bulletin*
737 *of the American Meteorological Society*, *72*(1), 2-20.
738
739 Schumacher, C., and R. A. Houze (2003), Stratiform rain in the tropics as seen by the
740 TRMM precipitation radar, *Journal of Climate*, *16*(11), 1739-1756.
741
742 Simpson, J., C. Kummerow, W. K. Tao, and R. F. Adler (1996), On the tropical rainfall
743 measuring mission (TRMM), *Meteorology and Atmospheric Physics*, *60*(1-3), 19-36.
744
745 Strahan, S. E., B. N. Duncan, and P. Hoor (2007), Observationally derived transport
746 diagnostics for the lowermost stratosphere and their application to the GMI chemistry and
747 transport model, *Atmospheric Chemistry and Physics*, *7*(9), 2435-2445.
748
749 Tian, B. J., B. J. Soden, and X. Q. Wu (2004), Diurnal cycle of convection, clouds, and
750 water vapor in the tropical upper troposphere: Satellites versus a general circulation
751 model, *Journal of Geophysical Research-Atmospheres*, *109*(D10), 16, DOI: D10101
752 10.1029/2003jd004117.
753

754 Waters, J. W., et al. (2006), The Earth Observing System Microwave Limb Sounder
755 (EOS MLS) on the Aura satellite, *Ieee Transactions on Geoscience and Remote Sensing*,
756 *44*(5), 1075-1092, DOI: 10.1109/tgrs.2006.873771.
757
758 Wilheit, T., L. J. Allison, and W. Shenk (1973), METEOROLOGICAL
759 INTERPRETATION OF NIMBUS-5 ELECTRICALLY SCANNING MICROWAVE
760 RADIOMETER IMAGES, *Bulletin of the American Meteorological Society*, *54*(10),
761 1117-1117.
762
763 Zhang, G. J., and N. A. McFarlane (1995), SENSITIVITY OF CLIMATE
764 SIMULATIONS TO THE PARAMETERIZATION OF CUMULUS CONVECTION IN
765 THE CANADIAN CLIMATE CENTER GENERAL-CIRCULATION MODEL,
766 *Atmosphere-Ocean*, *33*(3), 407-446.
767
768 Ziemke, J. R., J. Joiner, S. Chandra, P. K. Bhartia, A. Vasilkov, D. P. Haffner, K. Yang,
769 M. R. Schoeberl, L. Froidevaux, and P. F. Levelt (2009), Ozone mixing ratios inside
770 tropical deep convective clouds from OMI satellite measurements, *Atmospheric*
771 *Chemistry and Physics*, *9*(2), 573-583.
772
773 Zuidema, P. (1998), The 600-800-mb minimum in tropical cloudiness observed during
774 TOGA COARE, *Journal of the Atmospheric Sciences*, *55*(12), 2220-2228.
775
776 Figure Captions

777

778 Figure 1. GMI CO concentrations at middle and upper tropospheric levels, using one
779 month of daily output between 19°S-19°N. Panel (a) shows values from all grid boxes.
780 In subsequent panels, values from a grid box are only included if the convective
781 precipitation rate within that grid box meets the given threshold. The correlation of CO
782 between the two levels increases as the rain rate increases.

783

784 Figure 2. Each grid box shows the number of days (day count) in July 2007 for which
785 GEOS-4 computed a tropical convective rain rate satisfying the given threshold, at Aura
786 afternoon overpass times. Areas of most frequent convective rain correspond with well-
787 known areas of convection e.g. the ITCZ and the Maritime Continent. In panel (a), rain
788 rate $\geq$ 0.05 mm/hr, panel (b) $\geq$ 0.5 mm/hr, and panel (c) $\geq$ 1 mm/hr.

789

790 Figure 3. CO concentrations at middle vs. upper tropospheric levels, as measured in the
791 tropics (18°S-18°N) from Jan 2006 through Dec 2008. TES Global Survey data at 562
792 hPa were used, only where the Averaging Kernel diagonal was at least 0.085. MLS data
793 were used at 215 hPa, with values halved to compensate for a factor of 2 bias at this level.
794 The profiles were screened for quality and cloud presence as described in the text. Panel
795 (a) shows values from all qualifying profiles. In subsequent panels, a profile is only
796 included if the maximum local TRMM-based rain rate (within a 3x3 grid patch) meets the
797 given threshold. As the 3B-42 rain rate threshold increases, so too does the correlation of
798 CO between the two levels; at the same time, the number of points decreases pretty
799 dramatically. Histogram insets show the distribution of 1000 bootstrap test correlations,

800 ranging from -1 to 1. Markers below the histograms show the 5%, average, and 95%
801 locations; markers above show the correlation coefficients using all data.
802
803 Figure 4. Similar to Figure 2; however, this figure shows the geographic distribution of
804 TES/MLS profile pairs with TRMM rain rates satisfying thresholds 0.0, 0.05 and 1.0
805 mm/hr (panels (a) and (c) correspond to panels (a) and (b) in Figure 3). The profiles here
806 are binned at 2° x 2.5° to match Figure 2. In panel (a), no rain rate threshold is applied,
807 and the cloud-limiting filter for TES leaves clusters of profiles in areas of very little rain
808 (e.g. parts of Africa, Saudi Arabia and the South Atlantic). Panels (b) and (c) show the
809 effects of imposing rain rate thresholds of 0.05 and 1.0 mm/hr; this greatly reduces the
810 number of profiles, so a different color scale is used. As the required rain rate increases,
811 the remaining profiles are frequently located near areas of prominent rain (e.g. the ITCZ,
812 Maritime Continent, and Brazil).
813
814 Figure 5. Correlation of CO measurements from TES (562 hPa) and MLS (215 hPa),
815 plotted against rain rate thresholds satisfied by TRMM 3B-42. Four methods of rain rate
816 determination are shown in each panel; they differ only in the number of TRMM values
817 consulted in the vicinity of the TES/MLS observations, ranging from 77 (11x7) down to
818 9 (3x3). Each panel imposes a different AKD minimum for the TES data: 0.08, 0.085 and
819 0.09. Data spans three full years, 2006-2008. The points on the red/asterisk line (3x3
820 patches) in panel (b) correspond to the correlation coefficients shown in Table 1.
821 Correlation is not recorded if it does not satisfy the bootstrap criteria described in section
822 3.2.1.

Tables

Rain Rate Threshold (mm/hr)	0	0.5	1.0	1.5	2.0	2.5	3.0
Correlation Coefficient	0.454	0.538	0.604	0.618	0.719	0.780	0.804
Profile count	9940	213	108	64	45	33	22

Table 1. Interlevel CO Correlation Coefficients

CO correlations between middle and upper tropospheric levels associated with various rain rate thresholds. Cases shown include those from Figure 3 along with intermediate rain thresholds.

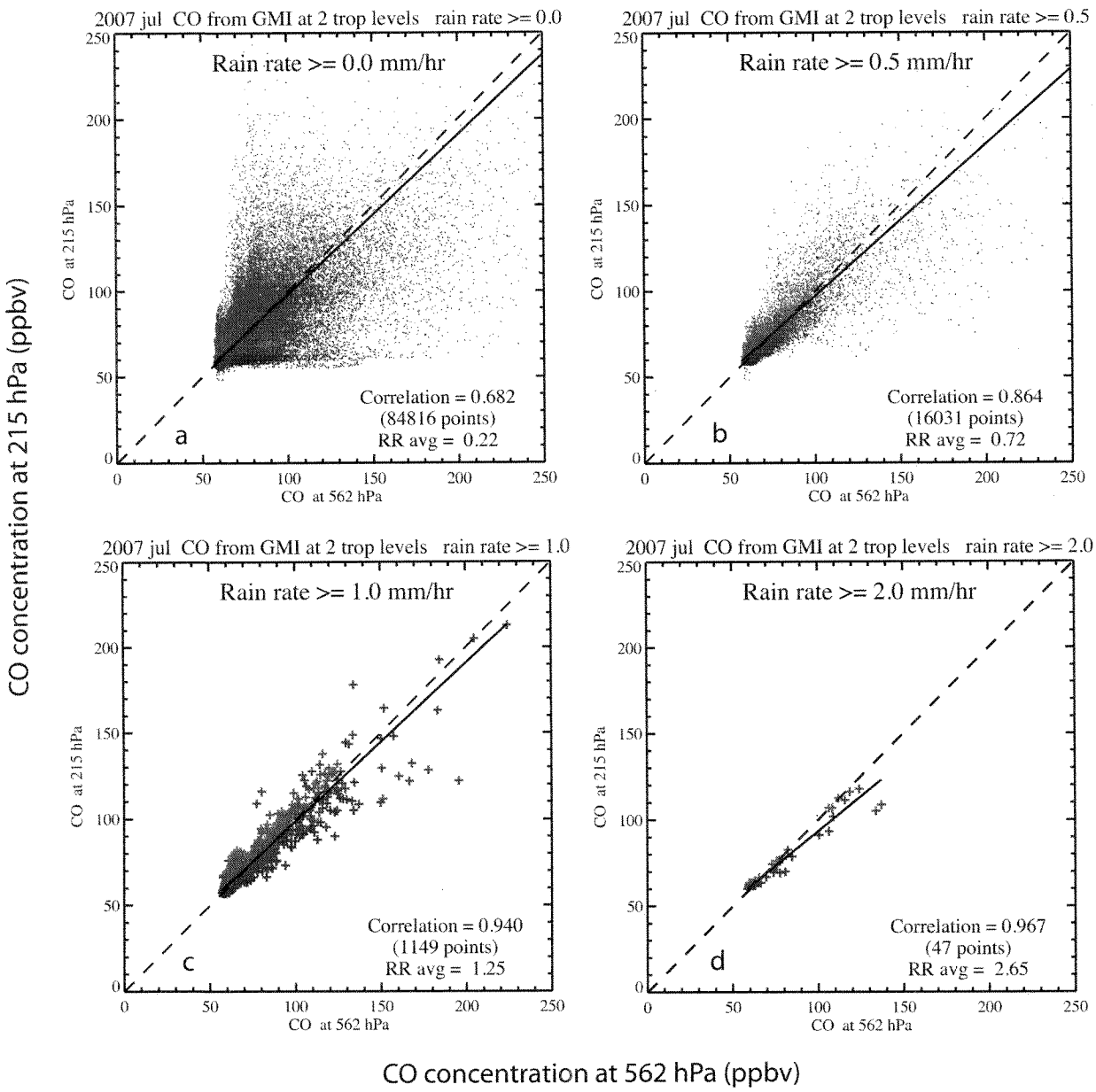
2007 jul CO from GMI at 2 trop levels rain rate >= 0.0
Rain rate >= 0.0 mm/hr
Correlation = 0.682
(84816 points)
RR avg = 0.22
a
2007 jul CO from GMI at 2 trop levels rain rate >= 0.5
Rain rate >= 0.5 mm/hr
Correlation = 0.864
(16031 points)
RR avg = 0.72
b
2007 jul CO from GMI at 2 trop levels rain rate >= 1.0
Rain rate >= 1.0 mm/hr
Correlation = 0.940
(1149 points)
RR avg = 1.25
c
2007 jul CO from GMI at 2 trop levels rain rate >= 2.0
Rain rate >= 2.0 mm/hr
Correlation = 0.967
(47 points)
RR avg = 2.65
d
CO at 215 hPa
CO at 562 hPa
0
50
100
150
200
250
CO concentration at 215 hPa (ppbv)
CO concentration at 562 hPa (ppbv)

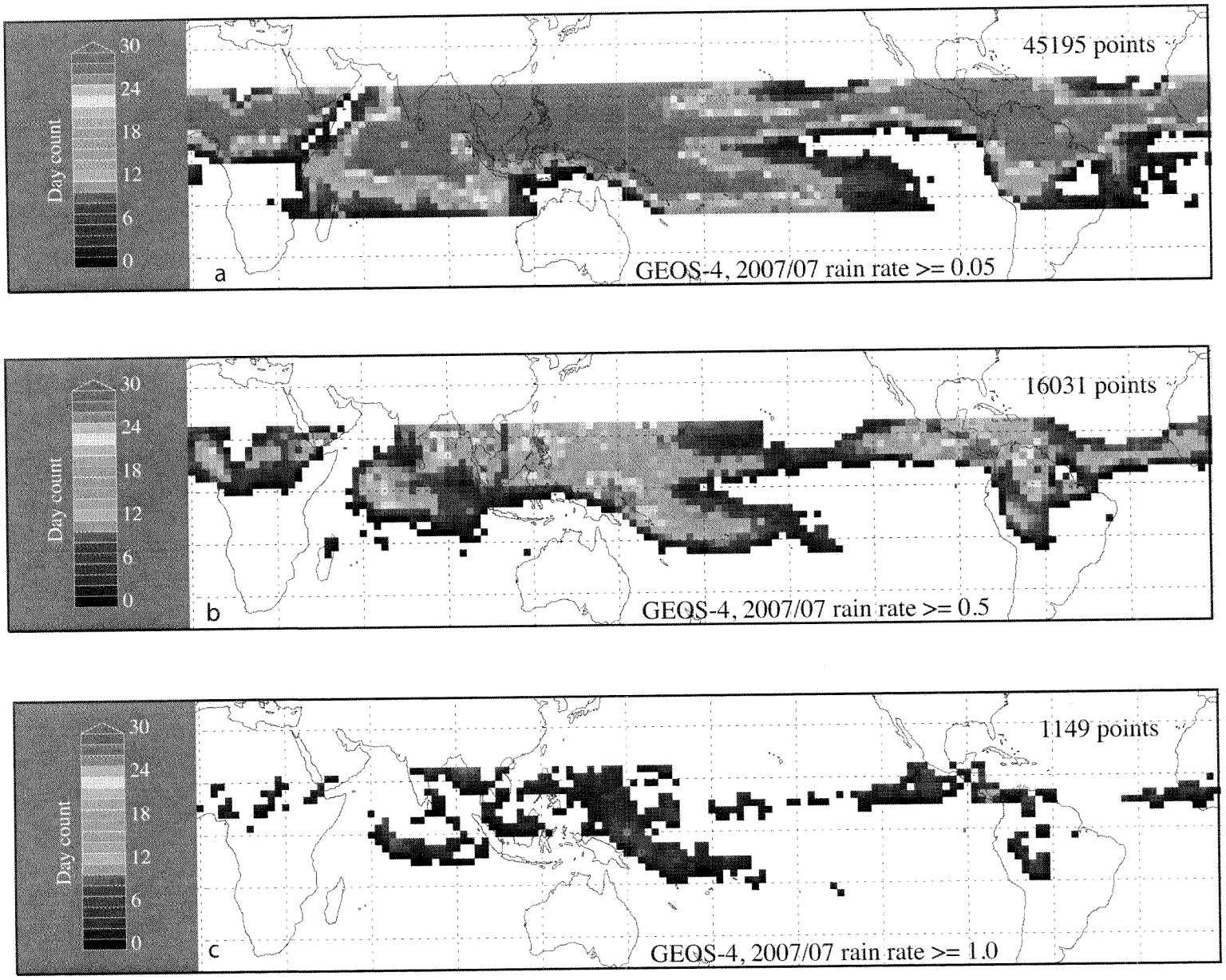
Day count
30
24
18
12
6
0
45195 points
a
GEOS-4, 2007/07 rain rate >= 0.05
Day count
30
24
18
12
6
0
16031 points
b
GEOS-4, 2007/07 rain rate >= 0.5
Day count
30
24
18
12
6
0
1149 points
c
GEOS-4, 2007/07 rain rate >= 1.0

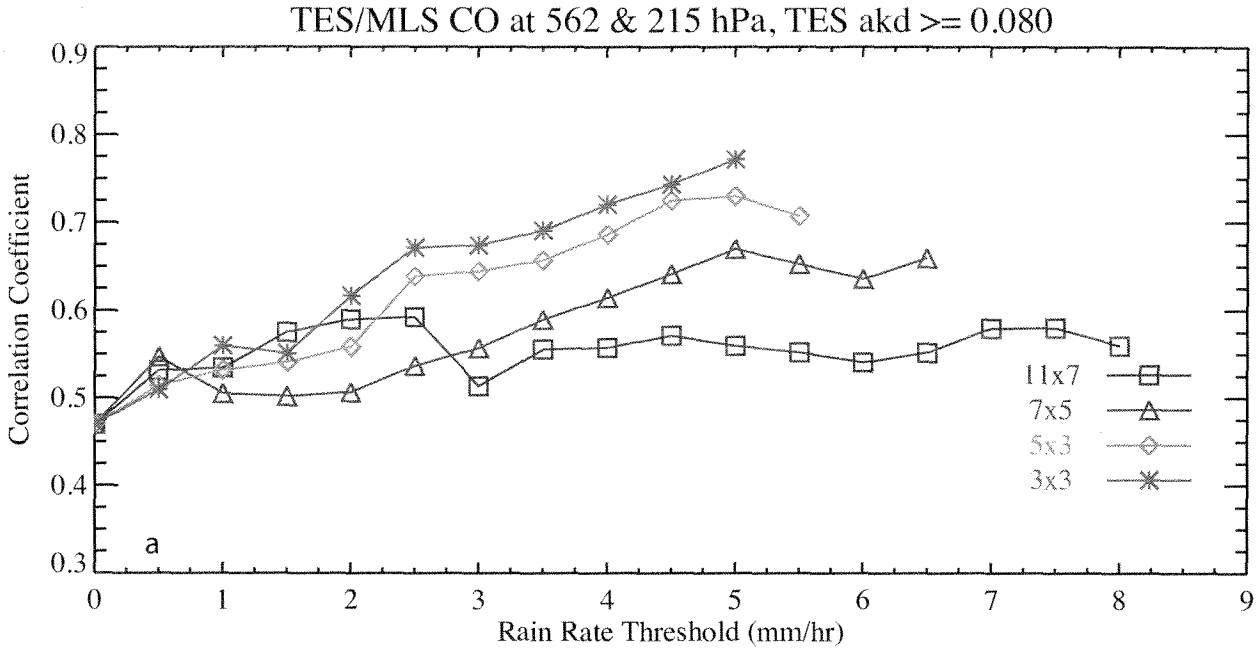
TES/MLS CO at 562 & 215 hPa, TES akd >= 0.080
Correlation Coefficient
Rain Rate Threshold (mm/hr)
11x7
7x5
5x3
3x3
a

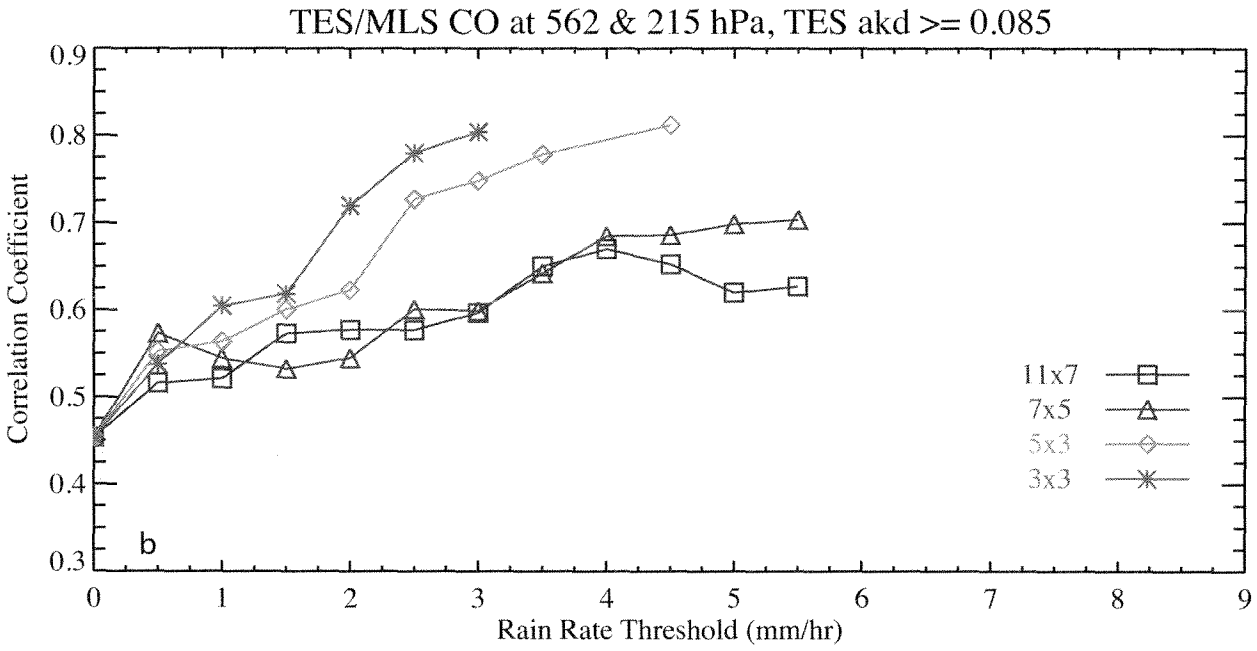
TES/MLS CO at 562 & 215 hPa, TES akd >= 0.085
Correlation Coefficient
Rain Rate Threshold (mm/hr)
11x7
7x5
5x3
3x3
b

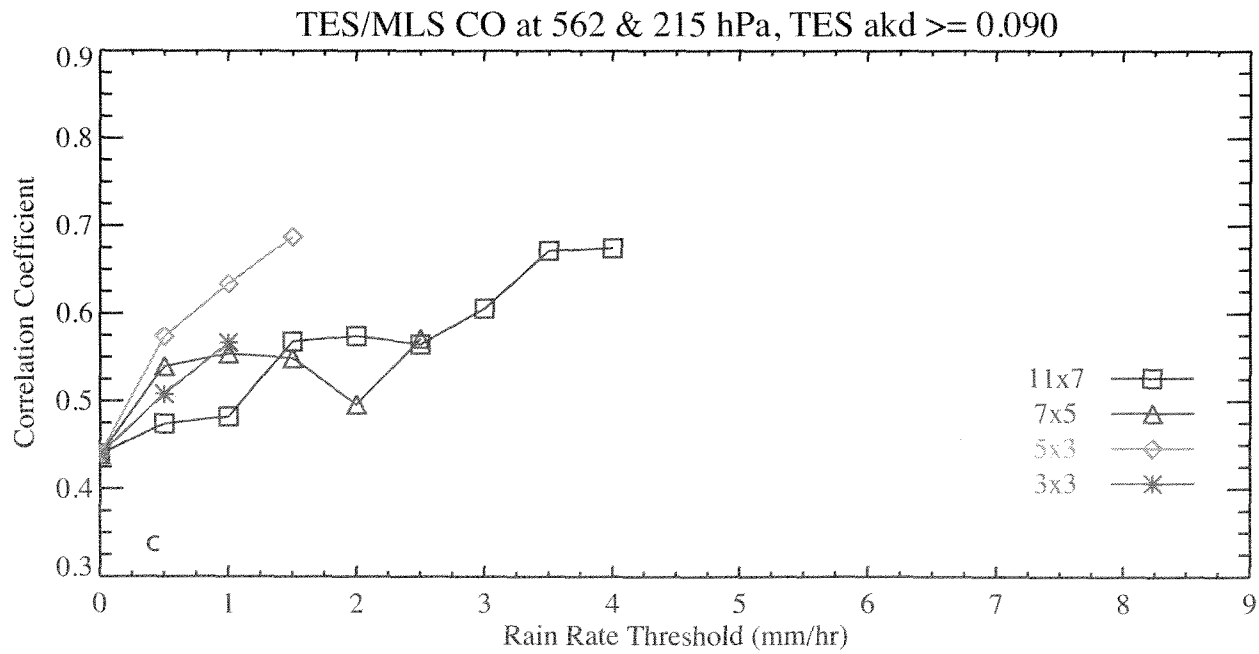
TES/MLS CO at 562 & 215 hPa, TES akd >= 0.090
Correlation Coefficient
Rain Rate Threshold (mm/hr)
11x7
7x5
5x3
3x3
c